Journal of Power Sources 194 (2009) 886–898

Contents lists available at ScienceDirect

Journal of Power Sources

journal homepage: www.elsevier.com/locate/jpowsour

Effects of operations and structural parameters on the one-cell stack performance of planar solid oxide fuel cell

Weisheng Xia [a,b,*], Yunzhen Yang [c], Wang Qiusheng [d]

[a] State Key Laboratory of Materials Processing and Die & Mould Technology, Huazhong University of Science and Technology, Wuhan 430074, PR China
[b] State Key Laboratory of Digital Manufacturing Equipment and Technology, Huazhong University of Science and Technology, Wuhan 430074, PR China
[c] College of Automotive Engineering, Wuhan University of Technology, Wuhan 430074, PR China
[d] School of Civil Engineering and Mechanics, Huazhong University of Science and Technology, Wuhan 430074, PR China

ARTICLE INFO

Article history:
Received 16 April 2009
Received in revised form 28 May 2009
Accepted 3 June 2009
Available online 11 June 2009

Keywords:
Planar solid oxide fuel cell
Flow uniformity
Thermo-fluid model
Temperature gradient
Thermoelectric characteristic

ABSTRACT

A three-dimensional mathematical model coupling the electrochemical kinetics with fluid dynamics is developed to simulate the heat and mass transfer in the one-cell stack of planar solid oxide fuel cells (SOFCs). Based on flow uniformity analysis, the distributions of temperature, current density, overpotential loss and other performance parameters in various operating parameters are obtained using a commercial CFD code (Fluent) coupled with the external subroutines programmed by VC++. Numerical flow data are observed in good agreement with experimental results reported in the literature. Results show that the one-cell stack in counter flow case has the advantages in better uniform current density and temperature distributions of PEN (Positive/Electrolyte/Negative) structure in the width direction, higher power output, fuel utilization factor and fuel efficiency than that in co-flow case. For counter flow case, better thermoelectric characteristics are observed in the temperature gradient, power output, fuel utilization factor and fuel efficiency with the decrease in the fuel inlet flow rate or the anode porosity. Increasing the air inlet flow rate and decreasing the fuel inlet temperature will reduce the temperature gradient; power output, fuel utilization factor and fuel efficiency are enhanced with the increase of the air inlet temperature and the decrease of the anode pore size and thickness.

1. Introduction

Solid oxide fuel cell (SOFC) has been considered as a promising alternative energy source device for residential and distributed power plants because of its high energy conversion efficiency and power density, low environmental hazards and potentially low production cost [1,2]. However, the further development of planar SOFCs faces the challenges related to maximize the power density and minimize the non-uniform temperature distribution, which contributes to the thermal stress in different SOFC components [3–5]. To optimize SOFC stack design and understand its complex operating mechanism, many challenges, such as heat and mass transfer together with electrochemical reactions, optimization of geometry and development of new materials, still remain to be solved step by step. The purpose of the optimal geometric design is also to get uniform distributions of air and fuel flows in order to improve the cell stack performance [6].

In the past, modelling the planar SOFC stack to study influences of various geometric and operating parameters on the stack performance has been carried out under the assumption of uniform flow velocity distributions in gas channels [7–11]. However, few investigations concerning the uniformity of air and fuel flows for U-type and Z-type SOFC stack have been reported [12,13]. Furthermore, quit a few researchers have also made an attempt to study the complex thermo-fluid electrochemical transport phenomena in planar SOFC stack with non-uniform gas flow rate in the stack direction and various interconnects [6,14].

Many researchers have discussed the influences of various operating parameters on SOFC performance, such as air and fuel flow rates, anode thickness, steam to carbon ratio, specific area, pre-reforming, and others [15–26]. Therefore, it is necessary to investigate effects of various geometric and operating parameters on the distributions of air and fuel flows, such as flow configuration, delivery rates of air and fuel, inlet temperatures of fuel and air, and anode thickness, pore size and porosity. Then, effects of the flow uniformity of the obtained air and fuel flow rates on the stack performance are simulated to predict the temperature and current density distributions, average temperature, average current density, air ratio, power output, fuel utilization factor and fuel efficiency during the operating process of SOFC stack.

* Corresponding author at: State Key Laboratory of Materials Processing and Die & Mould Technology, Huazhong University of Science and Technology, No. 1037, Luoyu Road, Wuhan 430074, PR China. Tel.: +86 27 8754 3493; fax: +86 27 8754 3493.
E-mail address: xiatianhust@hotmail.com (W. Xia).

0378-7753/$ – see front matter © 2009 Elsevier B.V. All rights reserved.
doi:10.1016/j.jpowsour.2009.06.009

Nomenclature

AH	air channel
a_k	polynomial coefficients
B	inertial coefficient
C_p	gas mixture's specific heat capacity ($J\,kg^{-1}\,K^{-1}$)
$C_{p,i}$	specific heat capacity of species *i* ($J\,kg^{-1}\,K^{-1}$)
d_p	average pore size of the electrodes (μm)
D_h	hydraulic diameter (m)
$D_{i,eff}$	effective diffusion coefficient of species *i* ($m^2\,s^{-1}$)
$D_{i,m}$	molecular diffusion coefficient of species *i* ($m^2\,s^{-1}$)
D_{Ki}	Knudsen diffusion coefficient of species *i* ($m^2\,s^{-1}$)
E	electromotive force (V)
F	Faraday constant ($C\,mol^{-1}$)
FH	fuel channel
i	local current density ($A\,m^{-2}$)
i_0	exchange current density ($A\,m^{-2}$)
$i_{0,a}$	anode exchange current density ($A\,m^{-2}$)
$i_{0,c}$	cathode exchange current density ($A\,m^{-2}$)
J_i	mass flux of species *i* ($kg\,m^{-3}\,s^{-1}$)
k	reaction rate constant ($mol\,m^{-3}\,Pa^{-2}\,s^{-1}$)
K	permeability coefficient (m^2)
L	cell stack length (mm)
M_i	molecular weight of species *i* ($kg\,mol^{-1}$)
M_m	average molecular weight ($kg\,mol^{-1}$)
n_{air}	air feed header inlet flow rate ($mol\,h^{-1}$)
n_e	electrons transferred per reaction
n_{fuel}	fuel feed header flow rate ($mol\,h^{-1}$)
p	pressure (Pa)
p_i	partial pressure of species *i* (Pa)
P_{SOFC}	power density of the cell ($W\,m^{-2}$)
Q	lower heating value
R	universal gas constant ($J\,mol^{-1}\,K^{-1}$)
R_j	ohmic resistivity (Ω m)
Re	Reynolds number
S	source term; effective temperature (K)
S_i	species source
S_m	mass source
$S_{T\text{-thermo}}$	energy source caused by thermodynamic reaction
$S_{T\text{-ohmic}}$	energy source caused by ohmic resistivity
S_v	momentum source
T	temperature (K)
T_{ave}	average temperature of PEN structure (K)
u	velocity of rib-channel ($m\,s^{-1}$)
U_{fuel}	fuel utilization factor
V	velocity vector ($m\,s^{-1}$)
v_k	velocity components in *k* direction ($m\,s^{-1}$)
V	local potential (V)
V_{cell}	output voltage (V)
W	cell stack width; width (mm)
y_i	molar fraction of species *i*
Y_i	mass fraction of species *i*

Greaks symbols

α_{im}	molar coefficient
β	transfer coefficient
δ_a	anode thickness (mm)
δ_c	cathode thickness (μm)
δ_e	electrolyte thickness (μm)
$\Delta h_{hyd\text{-}oxy}$	enthalpy change of H_2 oxidation reaction ($kJ\,mol^{-1}$)
$\Delta G_{hyd\text{-}oxy}$	Gibbs free enthalpy change of H_2 oxidation reaction ($kJ\,mol^{-1}$)
ε	porosity
ε_{SOFC}	fuel efficiency
Γ	degree of flow uniformity
η	overpotential (V)
κ_{eff}	effective thermal conductivity ($W\,m^{-1}\,K^{-1}$)
κ_f	thermal conductivity of multi-component mixture ($W\,m^{-1}\,K^{-1}$)
κ_i	thermal conductivity of species *i* ($W\,m^{-1}\,K^{-1}$)
κ_s	thermal conductivity of solid material ($W\,m^{-1}\,K^{-1}$)
λ_{air}	air ratio
μ_{eff}	effective dynamic viscosity ($kg\,m^{-1}\,s^{-1}$)
μ_i	dynamic viscosity of species *i* ($kg\,m^{-1}\,s^{-1}$)
ν	kinematic viscosity ($m^2\,s^{-1}$)
ρ	density ($kg\,m^{-3}$)
τ	tortuosity
α	heat transfer coefficient

Superscripts

in	feed conditions (fuel and air channel inlet)

Subscripts

a	anode
act	activation overpotential (V)
air	air gas channel; air feed header
ave	average value
bulk	bulk average in the cross-sectional area of the cell stack
c	cathode
con	concentration overpotential (V)
CO_2	carbon dioxide
e	electrolyte
f	fluid
fuel	fuel gas channel; fuel feed header
H_2; hyd	hydrogen
H_2O	steam
hyd-oxy	reaction of hydrogen and oxygen
int	interconnect
k	*x*, *y*, and *z* directions in Cartesian coordinates
n	total number of rib-channels
O_2; oxy	oxygen
rib	rib-channel
s	solid
TPB	three-phase boundary

This paper is to develop a comprehensive mathematical model on the basis of our original studies [27–33] to accomplish the simulation of the one-cell stack proposed by Yakabe et al. [34]. The present mathematical model cannot only be used to describe the physical–electrochemical phenomena in the unit cell, but also for the one-cell stack. Moreover, self-design methods are applied to solve the model. Subroutines programmed by VC++ are used to solve the electrochemical model because only the thermo-fluid model can be solved in the commercial software FLUENT. Finally, influences of the non-uniformity of gas flow rates on the thermal and electrical performance of the one-cell stack are analyzed.

2. Model development

2.1. Model description

The one-cell stack consists an interconnect structure and a three-layer region composed of two ceramic electrodes, anode and cathode, separated by a dense ceramic electrolyte (often referred to as PEN (Positive-electrode/Electrolyte/Negative-electrode)). The typical geometry of a planar SOFC proposed by Yakabe et al. [34]

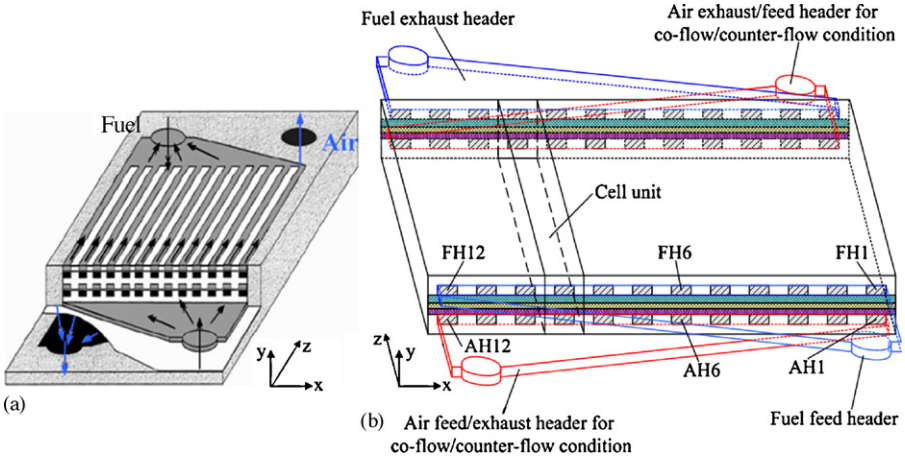

Fig. 1. The SOFC stack (a) proposed by Yakabe [34] and the one-cell stack in this study (b).

is depicted in Fig. 1a. The one-cell stack considered in this study is shown in Fig. 1b. The computational model is composed of nine components: (1) fuel feed header, (2) fuel exhaust header, (3) fuel-side interconnect with 12 rib-channels, (4) 12 fuel channels (FH1-FH12, the fuel channel (FH) on the right side is defined as FH1), (5) PEN structure, (6) 12 air channels (AH1-AH12, the air channel (AH) on the right side is defined as AH1), (7) air-side interconnect with 12 rib-channels, (8) air feed header and (9) air exhaust header. The schematic of the one-cell stack and its repeating cell unit presented in Fig. 1b is shown in Fig. 2. In this model, the thicknesses of anode, cathode, electrolyte and interconnect are 0.5 or 1.0, 0.25, 0.05 and 2.0 mm, respectively.

2.2. Thermo-fluid model

The physical–chemical transport phenomena in a SOFC system are strongly coupled. Hence, these phenomena are classified into the following categories: (1) mass transfer in gas feed/exhaust headers, gas channels and porous electrodes; (2) heat transfer in all constituent materials; (3) electrochemical reactions in the layers next to the interfaces between electrolyte and electrodes. In this study, the solid and fluid domains are all divided into some discrete meshes. As for each computational mesh, the conservation equations of mass continuity, momentum, energy and species are solved using the commercial software FLUENT code based on the finite volume method.

The mass continuity equation is written as

$$\nabla \cdot (\varepsilon \rho \boldsymbol{V}) = S_{\mathrm{m}} \tag{1}$$

where ε and V are the porosity of porous electrodes and the velocity vector, respectively. The governing equation is not only applicable to porous electrodes, but also gas channels including fuel and air channels. And ε is used to distinguish the porous electrodes and gas channels, in the channels $\varepsilon = 1$. Both air and fuel flows are considered as ideal gas mixtures, therefore, the effective density of the multi-components gas mixture based on ideal gas law (IGL) is given as follows [31]:

$$\rho = \frac{p}{RT}\left(\sum_k \frac{Y_k}{M_k}\right) \tag{2}$$

where p, R and T are the pressure, the universal gas constant and temperature, respectively. Y_k and M_k are the mass fraction and molecular weight of species k, respectively. S_{m} is the source term, which describes the change of species mass caused by electrochemical reactions. In this paper, the electrochemical reactions is assumed that only occur in the interfaces between the electrolyte and electrodes, so in the fuel and air channels, $\varepsilon = 1$ and $S_{\mathrm{m}} = 0$. And at the reaction layers next to the interfaces between electrolyte and

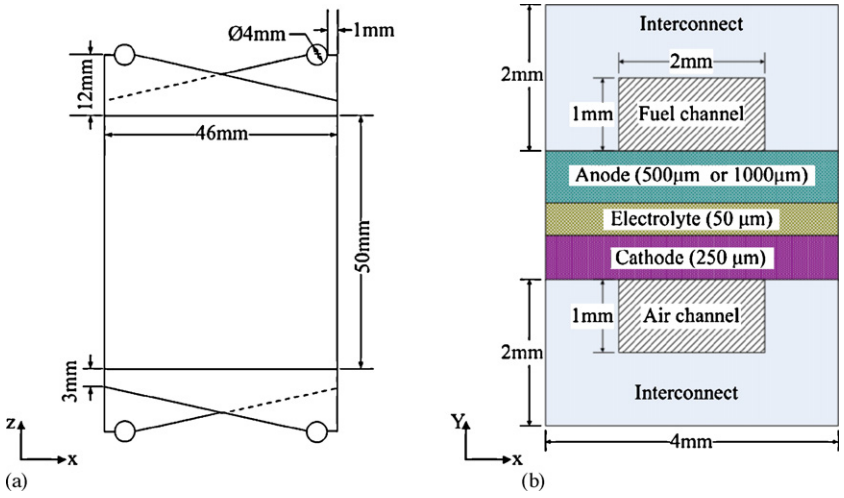

Fig. 2. Schematic of the one-cell stack (a) and the cross-sectional structure of the cell unit (b).

Table 1
Coefficients of Sutherland's viscosity law for different gas components [35].

Gas species	μ_0 (kg m^{-1} s^{-1})	T_0 (K)	S (K)
H_2	8.411E−6	273.11	96.67
H_2O	1.703E−5	416.67	861.11
CO_2	1.370E−5	273.11	222.22
O_2	1.919E−5	273.11	138.90
N_2	1.663E−5	273.11	106.67

porous electrodes S_m is as follows:

$$S_m = \sum_i J_i \quad i \in \{H_2, H_2O \text{ and } O_2\} \tag{3}$$

where J_i is the mass flux of species i during the electrochemical reaction process.

The momentum equation is as follows:

$$\nabla \cdot (\varepsilon \rho \boldsymbol{V}\boldsymbol{V}) = -\varepsilon \nabla p + \nabla \cdot (\varepsilon \mu_{\text{eff}} \nabla \boldsymbol{V}) + S_v \tag{4}$$

where μ_{eff} is the effective dynamic viscosity of the mixture gas, and is calculated by using ideal gas mixing law based on kinetic theory (MixKin) [30]:

$$\mu_{\text{eff}} = \sum_i \frac{y_i \mu_i}{\sum_k y_i \phi_{ik}} \tag{5}$$

$$\phi_{ik} = \frac{[1 + (\mu_i/\mu_k)^{1/2}(M_k/M_i)^{1/4}]^2}{[8(1 + (M_i/M_k))]^{1/2}} \tag{6}$$

where y_i is the mole fraction of species i. M_i and M_k are molecular weight of species i and k, respectively. μ_i and μ_k are dynamic viscosities of species i and k, respectively. In this study, the dynamic viscosities of gas components are defined as a function of temperature by using Sutherland's viscosity law, because the simulation of the SOFC stack involves heat transfer. Sutherland's viscosity law results from the kinetic theory by Sutherland (1893) using an idealized intermolecular-force potential. Sutherland's law with three coefficients is [35]:

$$\mu = \mu_0 \left(\frac{T}{T_0}\right)^{3/2} \frac{T_0 + S}{T + S} \tag{7}$$

where μ_0 is the reference value of viscosity. T_0 is a reference temperature, and S is an effective temperature, the Sutherland constant, which is characteristic of the gas. The parameters of Sutherland's law for gas components are listed in Table 1.

The momentum source in the porous electrodes, S_v, is calculated by the following formula:

$$S_v = -\left(\frac{\mu_{\text{eff}} \boldsymbol{V}}{K} + \varepsilon \rho B v_k \left|\boldsymbol{V}\right|\right) \tag{8}$$

where K is the porous electrode permeability, and v_k is the velocity component in the k direction. The first term on the right side of Eq. (8) accounts for the linear relationship between the pressure gradient and flow rate on the basis of the Darcy's law. The second term is the Forchheimer term concerning the inertial force effects [36]. In the fuel and air channels, $\varepsilon = 1$ and $S_v = 0$.

In general, gas species transfer mainly by convection in the flow channels and diffusion in the porous electrodes. The species conservation equation is

$$\nabla \cdot (\varepsilon \rho Y_i \boldsymbol{V}) = \nabla \cdot (\rho D_{i,\text{eff}} \nabla Y_i) + S_i \tag{9}$$

where Y_i is the mass fraction of species i. $D_{i,\text{eff}}$ is the effective gas diffusion coefficient of species i in the porous electrodes and fluid channels. Based on the dusty-gas model (DGM) [34,37], $D_{i,\text{eff}}$ in the porous electrodes can be expressed as follows:

$$D_{i,\text{eff}} = \frac{\varepsilon}{\tau}\left(\frac{1 - \alpha_{\text{im}} y_i}{D_{i,\text{m}}} + \frac{1}{D_{\text{Ki}}}\right)^{-1} \tag{10}$$

where τ is the tortuosity, $D_{i,\text{m}}$, y_i and D_{Ki} are the molecular diffusion coefficient, the molar fraction and the Knudsen diffusion coefficient of the species i, respectively. Here, α_{im} is defined as follows:

$$\alpha_{\text{im}} = 1 - \left(\frac{M_i}{M_m}\right)^{0.5} \tag{11}$$

where M_i is the molecular weight of species i, and M_m is average molecular weight. Knudsen diffusion occurs in the porous layer with small pores or under low pressure when the mean free-path of molecules is larger than the pore size, and the molecules collide with the walls more often than between themselves. The Knudsen diffusion coefficient for component i in the multi-components mixture is calculated based on the free molecule flow theory

$$D_{\text{Ki}} = \frac{1}{3}\left(\frac{8RT}{\pi M_i}\right)^{1/2} d_p \tag{12}$$

where d_p is the average pore size of the electrodes. In a multi-components gas system, the molecular diffusion coefficient of the component i is given by

$$D_{i,\text{m}} = \frac{1 - y_i}{\sum_{k \neq i}(y_k / D_{ik})} \tag{13}$$

where D_{ik} is the binary diffusion coefficient in the system with gas components i and k. S_i is the mass production/consumption rate of species i depending on electrochemical reactions. The production and/or consumption of reactants in a fuel cell are proportional to the electronic current produced by the electrochemical reaction. For hydrogen, oxygen and water species, the source and/or sink term in Eq. (9) can be expressed as follows:

$$S_{H_2} = -\frac{i}{2F} M_{H_2}, \quad S_{O_2} = -\frac{i}{4F} M_{O_2}, \quad S_{H_2O} = \frac{i}{2F} M_{H_2O} \tag{14}$$

where i is the charge-transfer current density. F is the Faraday constant. In the fuel and air channels, $\varepsilon = 1$ and $S_i = 0$.

The energy equation can be expressed as

$$\nabla \cdot (\rho C_p \boldsymbol{V} T) = \nabla \cdot (\kappa_{\text{eff}} \nabla T) + S_T \tag{15}$$

where C_p, κ_{eff} and S_T are the specific heat capacity of composition-dependent gas mixture, the effective thermal conductivity and the energy source term, respectively. The specific heat capacity of gas

Table 2
Polynomial coefficients for specific heat capacity of gas species [35].

	H_2O	H_2	CO_2	N_2	O_2
a_0	1.93780E+3	1.4147E+4	5.35446E+2	1.02705E+3	8.76317E+2
a_1	−1.18077	1.7372E−1	1.27867	2.16182E−2	1.22828E−1
a_2	3.64357E−3	6.9E−4	−5.46776E−4	1.48638E−4	5.58304E−4
a_3	−2.86327E−6	–	−2.38224E−7	−4.48421E−8	−1.20247E−6
a_4	7.59578E−10	–	1.89204E−10	–	1.14741E−9
a_5	–	–	–	–	−5.12377E−13
a_6	–	–	–	–	8.56597E−17

Table 3
Property parameters for different components of the cell unit [6,30–34,37,39].

Cell component	K ($m^2\,Pa^{-1}\,s^{-1}$)	κ ($W\,m^{-1}\,K^{-1}$)	ρ ($kg\,m^{-3}$)	R ($\Omega\,m$)	C_p ($kJ\,kg^{-1}\,K^{-1}$)
Anode	1.7×10^{-10}	6.23	7000	$2.98\times10^{-5}\exp(-1392/T)$	0.65
Cathode	1.7×10^{-10}	9.6	5620	1.2×10^{-4}	0.9
Electrolyte	–	2.7	5560	$3.0\times10^{-5}\exp(10300/T)$	0.3
Interconnect	–	13	7700	$5.0\times10^{-3}\exp(693.14/T)$	0.8

mixture is calculated as an average mass fraction of the pure species based on the mixing law [35]:

$$C_p = \sum_i Y_i C_{p,i} \tag{16}$$

where $C_{p,i}$ is the specific heat capacity of the individual species i in the gas mixture. The specific heat capacity of each species is calculated as a function of temperature:

$$C_{p,i} = \sum_{k=0}^{m} a_k T^k \tag{17}$$

where the polynomial coefficients, a_k, proposed by Rose and Cooper [35] are listed in Table 2. Heat transfer between the fluid and solid materials is limited to conduction and convection. The effect of radiation is neglected in this study because it is very small relative to the other kinds of heat transfer. Additionally, the effective thermal conductivities of porous electrodes are calculated by the following equation [31,38]:

$$\kappa_{eff} = \varepsilon\kappa_f + (1-\varepsilon)\kappa_s \tag{18}$$

where κ_f and κ_s are thermal conductivities of fluid and solid, respectively. The composition-dependent thermal conductivity for multi-components mixture κ_f is calculated by using ideal gas mixing law based on kinetic theory:

$$\kappa_f = \sum_i \frac{y_i\kappa_i}{\sum_k y_i\phi_{ik}} \tag{19}$$

where ϕ_{ik} is defined in Eq. (6). κ_i is thermal conductivity of species i. The thermal conductivity for each species is defined using kinetic theory as

$$\kappa_i = \frac{15}{4}\frac{R}{M_i}\mu_i\left[\frac{4}{15}\frac{C_{p,i}M_i}{R} + \frac{1}{3}\right] \tag{20}$$

The energy source term, S_T, mainly consists of reactions to release heat and ohmic heat. Based on the local current density, thermodynamic heat on the anode (except the ohmic heat) generated in the hydrogen oxidation reaction is calculated as follows:

$$S_{T\text{-thermo-a}} = i\left[\frac{\Delta h_{hyd\text{-}oxy}}{2F} - (E_{hyd\text{-}oxy} - \eta_{act} - \eta_{con})\right] \tag{21}$$

where the subscripts "hyd-oxy" indicates the hydrogen oxidation reaction. $\Delta h_{hyd\text{-}oxy}$ and $E_{hyd\text{-}oxy}$ are the enthalpy change and electromotive force (EMF) for hydrogen oxidation reaction, respectively. η_{act} and η_{con} are activation and concentration overpotentials of the electrodes, respectively. Ohmic heat in the electrolyte or in the electrodes is also locally calculated based on the ohmic resistivities and current densities. The ohmic heat sources on the anode, cathode and electrolyte are calculated as follows:

$$\begin{cases} S_{T\text{-ohmic-a}} = i^2 R_{j\text{-a}}\delta_{j\text{-a}} \\ S_{T\text{-ohmic-e}} = i^2 R_{j\text{-e}}\delta_{j\text{-e}} \\ S_{T\text{-ohmic-c}} = i^2 R_{j\text{-c}}\delta_{j\text{-c}} \end{cases} \tag{22}$$

where $R_{j\text{-a}}$, $R_{j\text{-e}}$, and $R_{j\text{-c}}$ are ohmic resistivities of anode, electrolyte and cathode, respectively. $\delta_{j\text{-a}}$, $\delta_{j\text{-a}}$ and $\delta_{j\text{-a}}$ are the thickness of anode, electrolyte and cathode, respectively. Hence, the heat sources on the anode, electrolyte and cathode are as follows:

$$\begin{cases} S_{T\text{-a}} = i\left[\dfrac{\Delta h_{hyd\text{-}oxy}}{2F} - (E_{hyd\text{-}oxy} - \eta_{act} - \eta_{con})\right] + i^2 R_{j\text{-a}}\delta_{j\text{-a}} \\ S_{T\text{-e}} = i^2 R_{j\text{-e}}\delta_{j\text{-e}} \\ S_{T\text{-c}} = i^2 R_{j\text{-c}}\delta_{j\text{-c}} \end{cases} \tag{23}$$

2.3. Materials and property settings

The anode (Ni/YSZ cermet) and cathode (doped lanthanum manganite, $LaMnO_3$) are modeled as porous media. The electrolyte (yttria-stabilized zirconia, ZrO_2–8 mol% Y_2O_3) and interconnect (magnesium-doped lanthanum chromium oxide ($LaMgCrO_3$)) are modeled as solid. The interface between electrodes and electrolyte are treated as the three-phase boundary (TPB). Firstly, all the faces in electrodes and electrolyte are numbered. If the coordinates of face center is same, the two faces are mapped and made as the interface between electrodes and electrolyte. Secondly, the each species of gas are numbered and to obtain the specious distributions in the interface. Finally, the thermo-fluid and electrochemical models are solved. In this paper, solid material properties used in this simulation are given in Table 3. The transport properties for the computational control volume in the present study are listed in Table 4.

2.4. Boundary conditions

The inlet flow rate into fuel and air feed headers, the inlet temperature and pressure, species concentration at fuel and air feed inlet, and output voltage are all summarized in Table 5. At the exhaust outlets of fuel and air, the fixed pressure boundary condition is adopted and fixed as 1 atm. The thermal boundary conditions at the top and bottom surfaces of the one-cell stack are regarded as thermally adiabatic. As it is difficult to determine the exact boundary condition at the other edge parts, the adiabatic boundary conditions are employed at the left and right edges. For the boundary between the solid and the fluid, the following continuity condition is imposed [34]:

$$[\kappa_{eff}(x)\nabla T_s(x)] \times n = \alpha[T_f(x) - T_s(x)] \tag{24}$$

where $\kappa_{eff}(x)$ is the thermal conductivity at x on the boundary, α is the heat transfer coefficient, n is the unit vector normal to the boundary, T_s and T_f are temperatures of the solid and fluid at x on the boundary, respectively.

Table 4
Transport property setting for computational control volume in the present simulation.

ρ ($kg\,m^{-3}$)	κ_{eff} ($W\,m^{-1}\,K^{-1}$)	C_p ($J\,kg^{-1}\,K^{-1}$)	μ_{eff} ($kg\,m^{-1}\,s^{-1}$)	$D_{i,eff}$ ($m^2\,s^{-1}$)
IGL	Eq. (18)	Mixing law	MixKin	DGM

IGL: ideal gas law; MixKin: ideal gas mixing law based on kinetic theory; DGM: dusty-gas model.

Table 5
Parameters and conditions in this study [6,23–26,39].

Description		Value
Species molar concentration at fuel feed inlet	Hydrogen, y_{H_2}	8/11
	Carbon dioxide, y_{CO_2}	2/11
	Water, y_{H_2O}	1/11
	Total	1.0
Species molar concentration at air feed inlet	Oxygen, y_{O_2}	0.21
	Nitrogen, y_{N_2}	0.79
	Total	1.0
Exchange current ($A\,m^{-2}$)	Anode, $i_{0,a}$	5300
	Cathode, $i_{0,c}$	2000
Inlet delivery rate ($m\,s^{-1}$)	Fuel feed header, V_{fuel}	0.6/1.8
	Air feed header, V_{air}	4.0/6.0
Inlet temperature (°C)	Fuel feed header, T_{fuel}	625/675
	Air feed header, T_{air}	625/675
Operating voltage (V)	V_{cell}	0.6
Operating pressure (kPa)	p	101.3
Porosity (%)	Anode, ε_a	0.45/0.25
	Cathode, ε_c	0.45/0.25
Tortuosity	Anode, τ_a	3.0
	Cathode, τ_c	2.0
Pore size of cathode (μm)	Anode, $d_{p,a}$	1.0/3.0
	Cathode, $d_{p,c}$	3.0
Length (mm)	Anode, l_a	50
	Cathode, l_c	50
	Electrolyte, l_e	50
Thickness (μm)	Cathode, δ_c	250
	Electrolyte, δ_e	50
	Anode, δ_a	500/1000
Cell unit number of the stack	n	12
Width (mm)	Stack, W	46
	Fuel channel in the cell unit, W_{FH}	2.0
	Air channel in the cell unit, W_{AH}	2.0
	Rib-channel, W_{rib}	2.0
Height (mm)	Fuel channel, d_{FH}	1.0
	Air channel, d_{AH}	1.0
	Rib-channel, d_{rib}	1.0
Diameter of gas inlet (mm)	Fuel feed/exhaust header and air feed/exhaust header	4.0

2.5. Electrochemical model

2.5.1. Reactions description

The oxidant reduction reaction occurring at the cathode is expressed as follows:

$$\tfrac{1}{2}O_2 + 2e^- \rightarrow O^{2-} \tag{25}$$

The oxygen ions transfer through the electrolyte and then into the active reaction layers of anode. The electrochemical reaction of fuel at the anode is

$$H_2 + O^{2-} \rightarrow H_2O + 2e^- \tag{26}$$

Hence, the overall reaction is

$$H_2 + \tfrac{1}{2}O_2 \rightarrow H_2O \tag{27}$$

2.5.2. Electrochemical reactions dynamics

According to the Faraday law, the reaction rates depend on the current density i [31]:

$$i = 2F\frac{df}{dt} = 4F\frac{dO_2}{dt} \tag{28}$$

where df/dt and dO_2/dt are the molar consumption rates of fuel and oxygen at the anode and the cathode, respectively.

During the energy transforming process, when the charge transfer reaction at the electrolyte–electrode interface is too slow to provide ions at the rate required by the demand of current, the activation polarization occurs and is defined by the Butler–Volmer equation [36]:

$$i = i_0\left\{\exp\left(\beta\frac{n_eF}{RT}\eta_{act}\right) - \left[-\exp(1-\beta)\frac{n_eF}{RT}\eta_{act}\right]\right\} \tag{29}$$

Then,

$$\eta_{act,a} = \frac{2RT}{n_eF}\sinh^{-1}\left(\frac{i}{2i_{0,a}}\right) \tag{30}$$

$$\eta_{act,c} = \frac{2RT}{n_eF}\sinh^{-1}\left(\frac{i}{2i_{0,c}}\right) \tag{31}$$

where β is the transfer coefficient ($0 < \beta < 1$), the transfer coefficient is considered to be the fraction of change in polarization that leads to a change in reaction rate constant, and its value is usually 0.5 for the fuel cell application [39], so $\beta \approx 0.5$ in this simulation, n_e is the number of electrons participating in the reaction, i_0 is the exchange current densities at the electrodes. $i_{0,a}$ and $i_{0,c}$ are the exchange current densities at the anode and the cathode, respectively. In this study, exchange current densities at the anode and the cathode are $5300\,A\,m^{-2}$ and $2000\,A\,m^{-2}$, respectively.

The concentration overpotential is defined as the difference between the EMF calculated based on the mean concentration overpotential E_{bulk} and that based on the local concentration on the TPB E_{TPB}

$$\eta_{con} = E_{bulk} - E_{TPB} = \frac{RT}{2F}\ln\left\{\frac{p_{O_2,bulk}}{p_{O_2,TPB}^{1/2}} \times \frac{p_{H_2,bulk} \times p_{H_2O,TPB}}{p_{H_2,TPB} \times p_{H_2O,bulk}}\right\} \tag{32}$$

where $p_{H_2,bulk}$ and $p_{H_2O,bulk}$ are the hydrogen and water partial pressures in fuel channel, respectively, and $p_{H_2,TPB}$ and $p_{H_2O,TPB}$ are those at the interface of electrolyte/anode, respectively. $p_{O_2,bulk}$ and $p_{O_2,TPB}$ are oxygen partial pressure in air channel and at the interface of electrolyte/cathode.

The local current density, i, and the ohmic losses, η_{ohm}, of the cell components are calculated by using Ohm's and Kirchhoff's law with the values of ohmic resistivity, R_j, as shown in Table 3:

$$\eta_{ohm} = \sum_j iR_j \quad j \in \{a, c, e \text{ and } int\} \tag{33}$$

The details of individual overpotentials above can be obtained from Suzuki et al. [38] and Chan et al. [39].

Finally, the following local relations exist among the electromotive force E, overpotential loss η, current density i, and the output voltage of the cell stack, V_{cell}:

$$E_{hyd\text{-}oxy} - (\eta_{act} + \eta_{con} + \eta_{ohm}) = V_{cell} \tag{34}$$

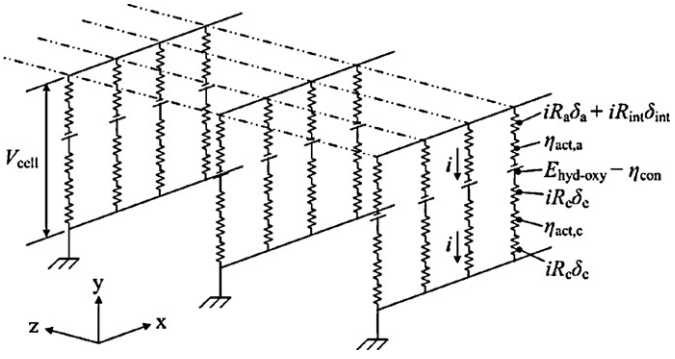

Fig. 3. Equivalent electrical circuit in the one-cell stack.

Table 6
Performance factors of the cell stack.

Fuel utilization factor
(36) $U_{\text{fuel}} = \frac{i_{\text{ave}} LW}{2F y^{\text{in}}_{\text{H}_2} n_{\text{fuel}}}$
Air ratio
(37) $\lambda_{\text{air}} = \frac{y^{\text{in}}_{\text{O}_2} n_{\text{air}}}{i_{\text{ave}} LW/(4F)}$
Power density
(38) $P_{\text{SOFC}} = i_{\text{ave}} V_{\text{cell}}$
Fuel efficiency
(39) $\varepsilon_{\text{SOFC}} = \frac{i_{\text{ave}} V_{\text{cell}} LW}{y^{\text{in}}_{\text{H}_2} Q^{\text{in}}_{\text{H}_2} n_{\text{fuel}}}$

where i_{ave} is the average total current density, L and W are the cell length and width, n_{air} and n_{fuel} are air and fuel feed header inlet flow rates, Q is lower heating value. The superscript in denotes feed conditions (fuel and air feed header inlet).

where $E_{\text{hyd-oxy}}$ is computed by Nernst equation:

$$E_{\text{hyd-oxy}} = -\frac{\Delta G_{\text{hyd-oxy}}}{2F} + \frac{RT}{2F}\ln\left(\frac{p_{\text{H}_2} p_{\text{O}_2}^{1/2}}{p_{\text{H}_2\text{O}}}\right) \quad (35)$$

where $\Delta G_{\text{hyd-oxy}}$ is the Gibbs's free-energy change of the hydrogen oxidation reaction, $p_{\text{H}_2\text{O}}$, p_{O_2} and p_{H_2} are the partial pressures of water gas, oxygen and hydrogen, respectively. The partial pressure of species i, p_i, is obtained as a product of the total local pressure and the molar fraction y_i.

If the output voltage of the cell stack V_{cell} is given, the local current density i can be obtained from these relations above, and vice versa. In the present model, the cell terminal voltage defined as V_{cell} is given as a signal to start the computation for different operating conditions (called operating voltage), and thereby both the current densities and potential fields are calculated based on an equivalent electrical circuit model illustrated in Fig. 3. In the one-cell stack, current is assumed to pass perpendicular to the gas flow direction through the anode, electrolyte, cathode and interconnector (including ribs). And this stack is divided into large number of the meshes. For the meshes with same centric coordinate in the PEN and interconnector (including ribs), the meshes are used to the circuit equivalent. Since the steady-state performance of the cell stack is discussed in the present study, the capacitance between the electrolyte and the electrodes is neglected.

2.6. Model performance factors

The fuel utilization factor is the fraction of the total inlet fuel consumed to produce electricity in the cell stack. The air ratio reflects the excess air, with respect to the stoichiometrically demand, otherwise the excessive will cooling the cell stack. Table 6 presents the mathematical definition of these performance factors.

2.7. Model calculation process

The governing Eqs. (1), (4), (9) and (15), together with their relevant boundary conditions and initial conditions, are solved with computational fluid dynamics software FLUENT by finite volume method coupling the electrochemical Eq. (32). The modelling domain consists of the fuel feed/exhaust headers, fuel channel, air feed/exhaust headers, air channel, interconnect and PEN structure, as shown in Fig. 1. All the source terms in the mass continuity, species conservation and energy equations must be adopted in the electrochemical model because this model is coupled with the thermo-fluid one. Moreover, the electrochemical model must be solved by the subroutines developed in this study, and the model is not only originated from the software Fluent.

The finite-volume Navier–Stokes and transport equations are solved to obtain the gas species concentrations, velocities and temperatures at each computational control volume in the one-cell stack. These information are supplied for the electrochemical model to calculate the local current density, and this model is processed by the self-developed subroutine interface using the user defined function (UDF) provided by FLUENT. Then, the resultant current density is applied to obtain the hydrogen reaction rate, heat source and species sources. Gas species concentrations, velocities and temperature distributions are calculated for the next iteration, and so on, until the convergence of solution is achieved.

All the cases in this study are shown in Table 7, and the rest operating conditions and parameters are listed in Table 5.

3. Results and discussion

3.1. Effects of flow patterns on the cell stack performance based on flow uniformity analysis

Fig. 4 shows the velocity distributions in fuel and air channels for counter flow in case 1 and co-flow in case 2 (Table 7). In this figure, u_i is the velocity at the ith rib-channel, and u_{ave} is the averaged mean velocity of all the channels. The flow rates at the channels close to the entrance and exist of the gas feed/exhaust headers are higher than those in the middle channels both in counter flow and co-flow conditions.

For quantitative estimation, the degree of flow uniformity is defined as follows [6]: $\Gamma = 1 - \{(1/n)\sum_{i=1}^{n}((u_i - u_{\text{ave}})/u_{\text{ave}})^2\}^{1/2}$, where $n = 12$ denotes the total number of rectangular rib-channels in the one-cell stack.

As for the two flow configurations calculated, the cell stack operating in counter flow case has a more uniform flow velocity distribution in both fuel and air channels. As for the counter flow condition in case 1, the degrees of flow uniformity in fuel and air channels are 0.9620 and 0.8985, respectively. Accordingly, the degrees in fuel and air channels are 0.9289 and 0.8970 under co-flow condition in case 2, respectively.

Table 7
Computational parameters for all the calculated cases.

Case	1	2	3	4	5	6	7	8	9
Flow pattern	Counter flow	**Co-flow**	Counter flow	Counter low	Counter flow	Counter flow	Counter flow	Counter flow	Counter flow
Air inlet velocity, V_{air} (m s^{-1})	6.0	6.0	**4.0**	6.0	6.0	6.0	6.0	6.0	6.0
Fuel inlet velocity, V_{fuel} (m s^{-1})	0.6	0.6	0.6	**1.8**	1.8	1.8	1.8	1.8	1.8
Air inlet temperature, T_{air} (°C)	625	625	625	625	**675**	625	625	625	625
Fuel inlet temperature, T_{fuel} (°C)	625	625	625	625	625	**675**	625	625	625
Porosities of anode and cathode, ε (%)	45	45	45	45	45	45	**25**	45	45
Pore size of the anode, $d_{\text{p,a}}$ (μm)	3.0	3.0	3.0	3.0	3.0	3.0	3.0	**1.0**	3.0
Anode thickness, δ_{a} (μm)	500	500	500	500	500	500	500	500	**1000**

Values in bold of Cases 2–4 are differences from those of the case 1, and values in bold of cases 5–9 are differences from those of the case 4.

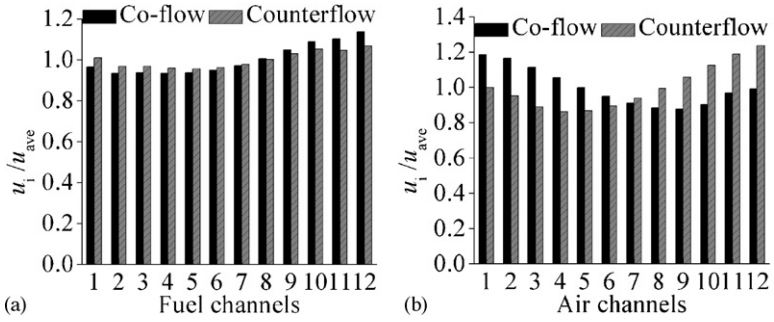

Fig. 4. Velocity distributions in fuel (a) and air channels (b) for counter flow in case 1 and co-flow in case 2 listed in Table 7.

Table 8
Cell stack performance.

Cases	$E_{hyd\text{-}oxy}$ (V)	η_{act} (V)	η_{con} (V)	η_{ohm} (V)	T_{ave} (K)	i_{ave} (A m^{-2})	P_{SOFC} (W m^{-2})	U_{fuel} (%)	λ_{air}	ε_{SOFC} (%)
1	0.9530	0.2354	0.0098	0.1078	1057.2	4156.6	2494.0	66.6	8.7	31.9
2	0.9619	0.2253	0.0094	0.1272	1041.4	4022.8	2413.7	64.4	9.0	30.8
3	0.9240	0.2616	0.0105	0.0519	1148.6	4267.4	2560.4	68.4	5.6	32.7
4	0.9916	0.2748	0.0147	0.1021	1081.9	4873.8	2924.3	26.0	7.4	12.5
5	0.9766	0.2952	0.0154	0.0659	1137.3	5009.7	3005.8	26.7	7.2	12.8
6	0.9876	0.2775	0.0146	0.0955	1090.7	4883.1	2929.9	27.5	7.0	13.2
7	0.9941	0.2671	0.0230	0.1040	1076.4	4737.1	2842.3	25.3	7.6	12.1
8	0.9892	0.2824	0.0061	0.1007	1078.1	5013.8	3008.3	26.7	7.2	12.8
9	0.9957	0.2663	0.0170	0.1124	1069.3	4754.5	2852.7	25.4	7.6	12.2

Current density distributions for counter flow in case 1 and co-flow in case 2 are shown in Fig. 5, and their temperature distributions of PEN structure are shown in Fig. 6. The average values of voltage, current density and the temperature of PEN structure for all the calculated cases are itemize in Table 8 as well as power density, fuel utilization factor, air ratio and fuel efficiency.

In the counter flow case, the current density decreases along the fuel flow direction, and is high near the fuel inlet due to the high temperature leading to small ohmic overpotential and Nernst potential in that region. This is because EMF gradually decreases from fuel inlet toward outlet as O_2 and H_2 are consumed and H_2O is produced. In contrast, the maximum current density appears in the middle of the cell stack in the co-flow case. This is because the overpotentials are very temperature sensitive and there is a trade-off between the temperature increase and the reactant concentration decrease. The characteristics of current density in both the two flow cases are similar to those of the planar one-cell stack with uniform flow rates in fuel and air inlets [11]. In addition, the characteristic in co-flow case is similar to that of the planar cell unit [34,36]. Compared with the co-flow case, the current density distribution in counter flow case is more uniform in the width direction of the cell stack due to the better uniform fuel and air flows. The high current densities appear in the location where are channels with large fuel delivery rate. From Table 8, it is suggested that the average current density, power density, fuel utilization factor and fuel efficiency for counter flow case in case 1 are higher than those for co-flow case in case 2.

The average temperature of PEN structure is 1057.2 K in counter flow case shown in Table 8. Furthermore, the PEN structure temperature rises rapidly in the air flow direction, reaching a maximum

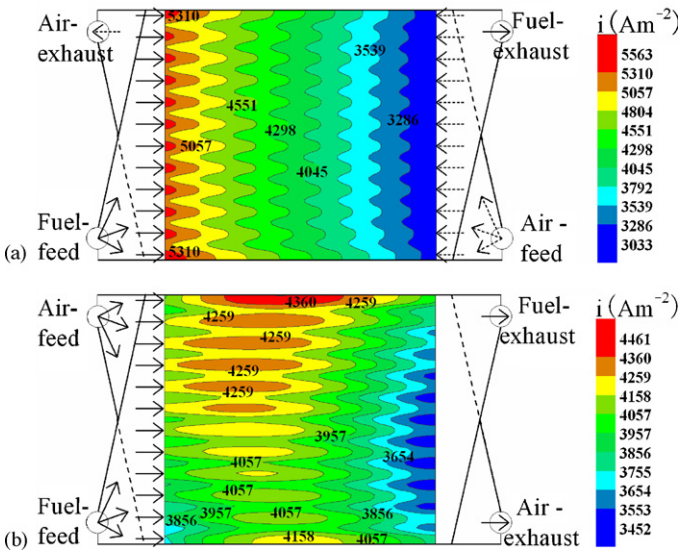

Fig. 5. Current density distributions for counter flow in case 1 (a) and co-flow in case 2 (b) listed in Table 7.

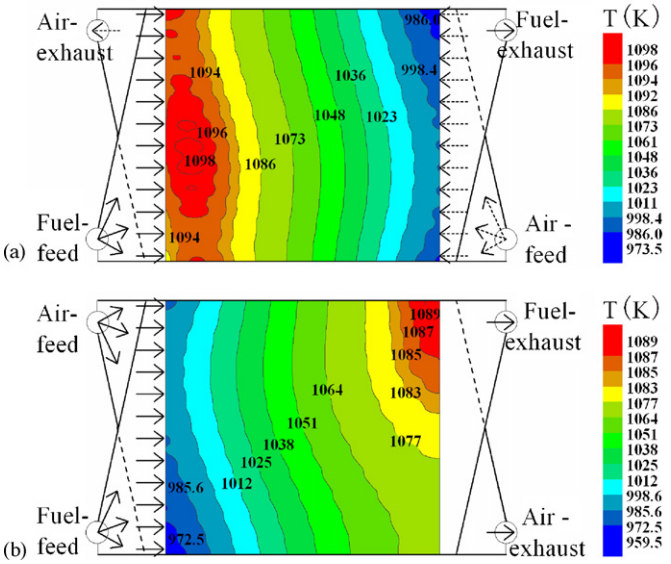

Fig. 6. Temperature distributions of PEN structure for counter flow in case 1 (a) and co-flow in case 2 (b) listed in Table 7.

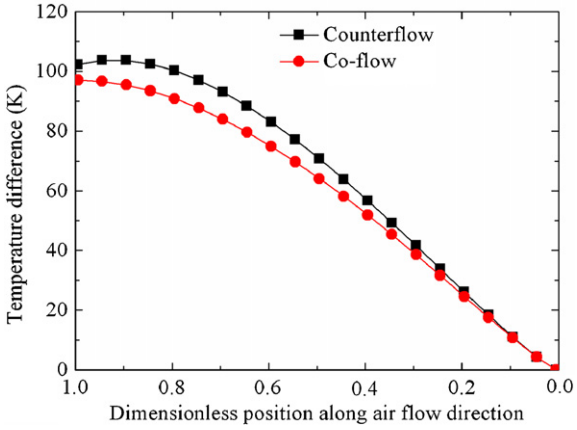

Fig. 7. Averaged temperature difference of PEN structure for counter flow in case 1 and co-flow in case 2.

near the fuel inlet, and then gradually drops. Air flow has most effectively cooling effect near the air inlet, and carries heat generated in the PEN structure, and thus moves the hotspot toward the air outlet. The average temperature of PEN structure is 1041.4 K in co-flow case. However, it rises uniformly along the direction of fuel flow, and is highest near the fuel outlet close to fuel exhaust header, as shown in Fig. 7. The temperature gradient of PEN structure in co-flow case is smaller than that in counter flow case from air inlet to outlet. This is due to the offsetting effects of air near the inlet, at its coolest, being aligned with the fuel inlet.

Compared with co-flow case, it is should be noted that the temperature distribution of PEN structure for counter flow case is more uniform in the width direction of the cell stack. This is because the better uniform fuel and air flows leading to better current density distribution. The high temperature of PEN structure is intensively concentrated in the regions close to the fuel exhaust header. The temperature characteristics of PEN structure in counter flow case are similar to those of planar one-cell stack with uniform flow rates in fuel and air inlets [11]. In addition, the characteristics in co-flow case is similar to the relevant findings in the literature [31,31,34,36]. The results in counter flow case are also similar to that of the planar cell unit [30,31].

As a conclusion, the cell stack in counter case has a better performance (such as average current density, power density, fuel utilization factor, fuel efficiency and so on) than that in co-flow case. To achieve a more uniform PEN structure temperature distribution, a deeply investigation into the effect of operating conditions, physical and structural parameters of the cell stack on its performance based on flow uniformity analysis in counter case is described in the follows.

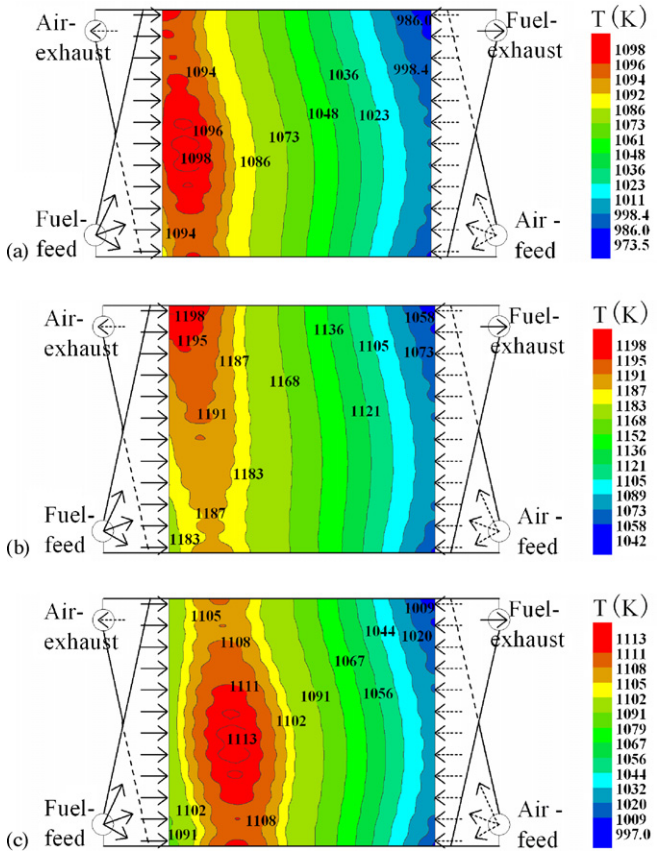

Fig. 9. Temperature distributions of PEN structure for counter flow in case 1 (a), case 3 (b) and case 4 (c) with different air inlet flow rates.

3.2. *Effects of inlet velocity on the cell stack performance based on flow uniformity analysis*

The velocity distributions in fuel and air channels and temperature distributions of PEN structure along the air flow direction for cases 1, 3 and 4 are illustrated in Figs. 8–10, as well as the details of average temperature difference of PEN structure.

As shown in Fig. 8, the degrees of flow uniformity in different fuel channels decrease from 0.9620 to 0.9537 and 0.9429 with the decrease of air inlet velocity and the increase of fuel inlet velocity. Meanwhile, the degrees of flow uniformity in air channels slightly increase from 0.8985 to 0.9034 and 0.9010 when the air inlet velocity decreases and the fuel inlet velocity increases. Consequently, fuel flows are less uniform with the decrease of air inlet velocity and the increase of the fuel inlet velocity.

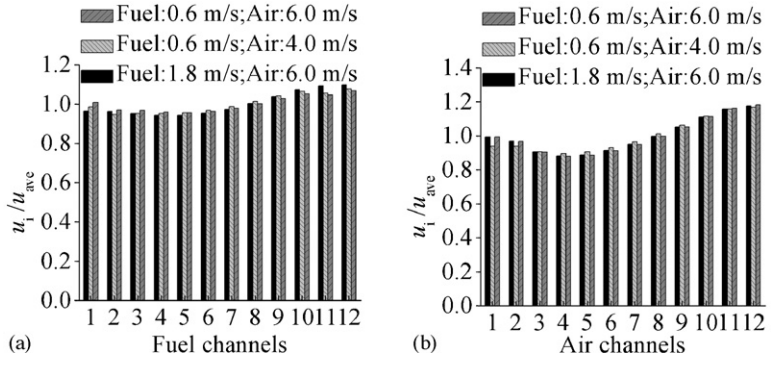

Fig. 8. Velocity distributions in fuel (a) and air channels (b) for counter flow in cases 1, 3 and 4 listed in Table 7.

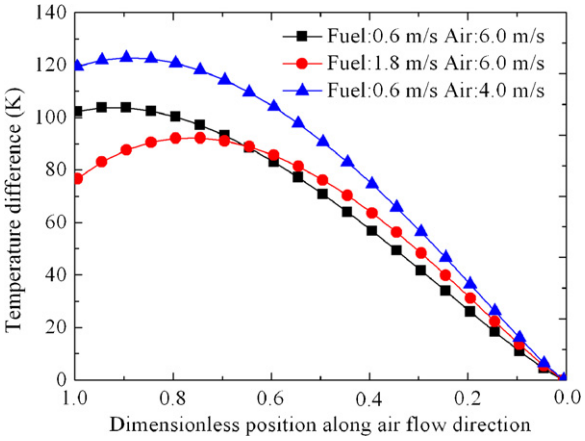

Fig. 10. Averaged temperature difference of PEN structure for counter flow in cases 1, 3 and 4 listed in Table 7.

As listed in Table 8, the average temperature of PEN structure rises from 1057.2 K to 1148.6 K when the air inlet velocity decreases from 6.0 m s^{-1} to 4.0 m s^{-1}. The average current density increases from 4156.2 A m^{-2} to 4267.4 A m^{-2} with the decrease of air inlet velocity due to the ohmic overpotential decrease with the increase of PEN structure temperature. Moreover, the power density, fuel utilization factor and fuel efficiency all increase with the decrease of air inlet velocity. It is to be noted that the decrease of air ratio is the reason why the average temperature of PEN structure rises with the decrease of air inlet velocity. The average temperature of PEN structure rises from 1057.2 K to 1081.9 K when the fuel inlet velocity increases from 0.6 m s^{-1} to 1.8 m s^{-1}, which is because more heat produced by H_2 oxidation reaction. The reaction is promoted by the increase of average current density with enhanced electrochemical reactions by the more fuel supply. With the increase of fuel inlet velocity, the power density increases, but the air ratio, fuel utilization factor and fuel efficiency decrease.

It can be observed in Fig. 9 that the distribution of PEN structure temperature is less uniform with the decrease of air inlet velocity and the increase of the fuel inlet velocity due to the worse uniformity of fuel flows. The temperature difference of PEN structure in the width direction of the cell stack increases with the decrease of air inlet velocity, and the high temperature region expands with the increase of fuel inlet velocity.

Fig. 10 presents the average temperature difference of PEN structure in the air flow direction for cases 1, 3 and 4. The temperature gradient of PEN structure increases when air inlet velocity decreases or fuel inlet velocity increases.

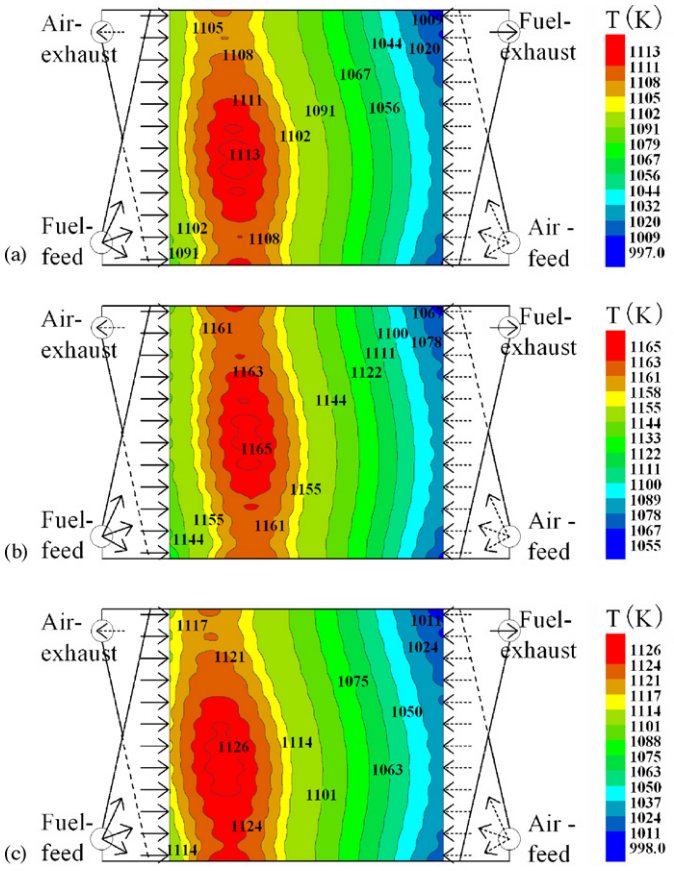

Fig. 12. Temperature distributions of PEN structure for counter flow in case 4 (a), case 5 (b) with higher air inlet temperature and case 6 (c) with higher fuel inlet temperature listed in Table 7.

3.3. *Effects of inlet temperature on the cell stack performance based on flow uniformity analysis*

Velocity distributions in fuel and air channels and temperature distributions of PEN structure are illustrated in Figs. 12 and 13, as well as the details about the average temperature difference of PEN structure along the air flow direction for cases 4–6.

As shown in Fig. 11, the degree of flow uniformity decreases from 0.9429 to 0.9316 in fuel channels, and increases from 0.9010 to 0.9104 in air channels with the increase of air inlet temperature. On the contrary, with the increase of fuel inlet temperature, the degree in fuel channels increases from 0.9429 to 0.9537, and decreases from 0.9010 to 0.8967 in air channels. Therefore, air flows are more uniform with the increase of air inlet temperature. Oth-

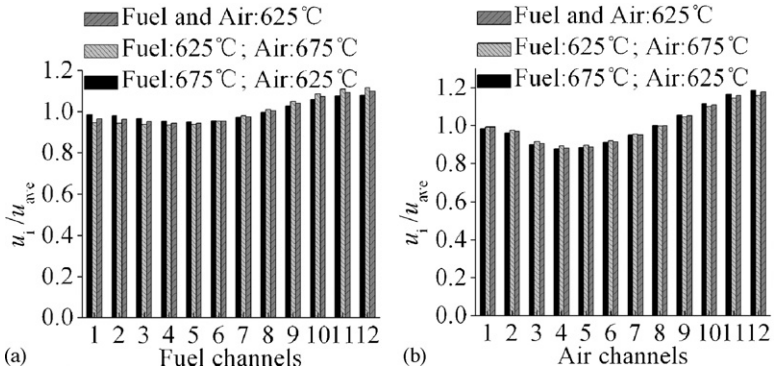

Fig. 11. Velocity distributions in fuel (a) and air channels (b) for counter flow in cases 4–6 listed in Table 7.

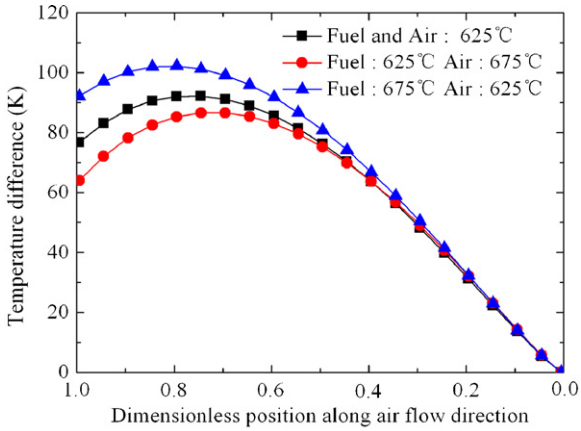

Fig. 13. Averaged temperature difference of PEN structure for counter flow in cases 4–6 listed in Table 7.

erwise, they are less uniform with the increase of the fuel inlet temperature.

As listed in Table 8, the average temperatures of PEN structure rise from 1081.9 K to 1137.3 K and 1090.7 K, when the air and fuel inlet temperatures increase from 625 °C to 675 °C, respectively. The average current densities increase from 4873.8 A m^{-2} to 5009.7 A m^{-2} and 4883.1 A m^{-2} with the increase of air and fuel inlet temperatures, respectively, which is because the ohmic overpotential decreases due to the increase of PEN structure temperature. Moreover, the power density, fuel utilization factor and fuel efficiency increase with the increase of air and fuel inlet temperatures.

Fig. 12 shows that the distribution of PEN structure temperature is more uniform in the width direction of the cell stack with the increase of air inlet temperature. This case is due to the better uniform air flows. With the increase of fuel inlet temperature, the temperature difference is almost constant in the width direction of the cell stack.

Fig. 13 presents the average temperature difference of PEN structure in the air flow direction for cases 4–6 in details. The temperature gradient of PEN structure increases with the individual increase of air and fuel inlet temperatures. It is to be noted that the decrease of air ratio and the increase of average current density are the reasons why the temperature gradients of PEN structure increase with the increase of air and fuel inlet temperatures. In the higher air inlet temperature case (case 5), the ascending of the average temperature gradient is 2.49 K mm^{-1}, and the descending is 1.77 K mm^{-1}. If the cell stack operates on the condition that the ascending of average temperature gradient is less than its descending, more uniform PEN structure temperature distribution may be achieved in the width direction of the cell stack, as well as higher power output, fuel utilization factor and fuel efficiency.

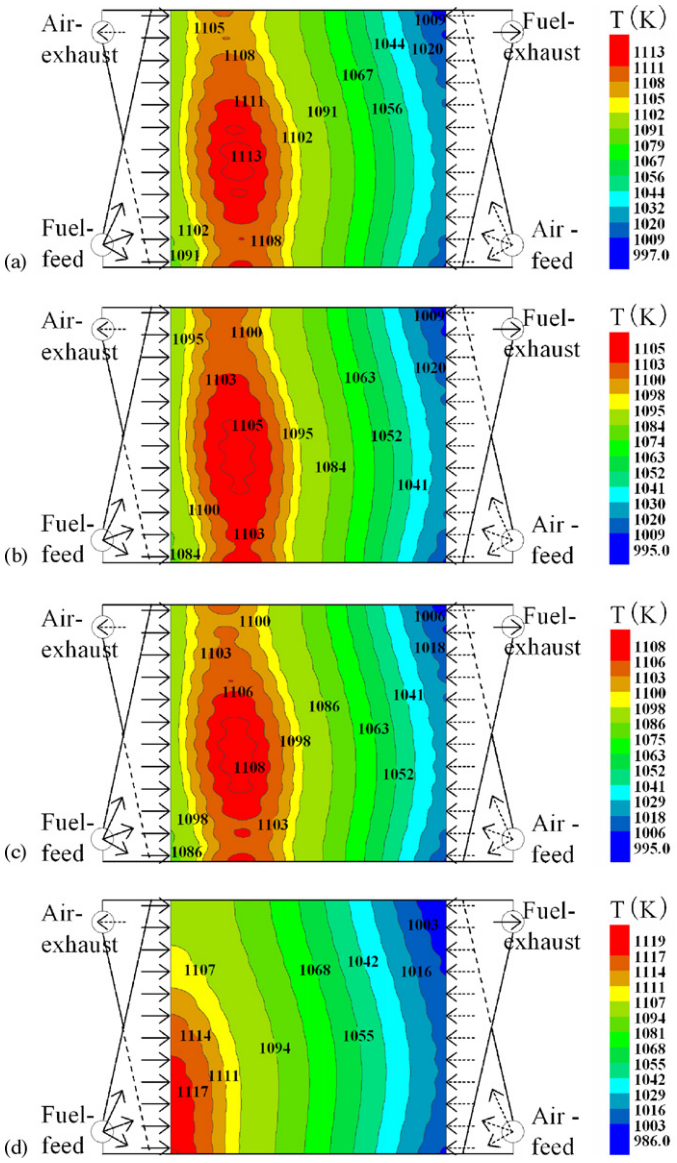

Fig. 15. Temperature distributions of PEN structure for counter flow in case 4 (a), case 7 (b) with lower porosities of electrodes, case 8 (c) with smaller pore size of anode and case 9 (d) with thicker anode thickness listed in Table 7.

3.4. Effects of physical and structural parameters on the cell stack performance based on flow uniformity analysis

Velocity distributions in fuel and air channels and temperature distributions of PEN structure along the air flow directions are shown in Figs. 14–16, as well as the details about the average

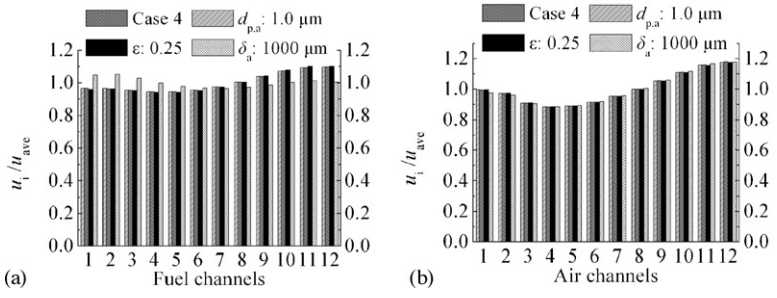

Fig. 14. Velocity distributions in fuel (a) and air channels (b) for counter flow in cases 4, 7–9 listed in Table 7.

temperature difference of PEN structure for cases 4, 7–9, respectively.

As shown in Fig. 14, the degree of flow uniformity in fuel channels decreases from 0.9429 to 0.9392, and increases from 0.9010 to 0.9027 in air channels with the decrease of anode porosity. The degrees increase from 0.9429 and 0.9010 to 0.9439 and 0.9019 with the decrease of anode pore size in fuel and air channels, respectively. The degree increases from 0.9429 to 0.9715 in fuel channels, and decreases from 0.9010 to 0.8995 in air channels with the increase of anode thickness. In conclusion, air flows are more uniform with the decrease of anode porosity and its pore size, but are less uniform with the increase of anode thickness.

As listed in Table 8, the average temperatures of PEN structure decline from 1081.9 K to 1076.4 K, 1078.1 K and 1069.3 K when the anode porosity and pore size decrease, and the anode thickness increases. The average current densities decrease from 4873.8 A m^{-2} to 4737.1 A m^{-2} and 4754.5 A m^{-2} because of the larger concentration overpotentials with the decrease of anode porosity and the increase of anode thickness. Furthermore, the power density, fuel utilization factor and fuel efficiency decrease with the decrease of anode porosity and the increase of anode thickness. The average current density increase from 4873.8 A m^{-2} to 5013.8 A m^{-2} owing to the smaller concentration overpotentials when anode pore size decreases. To sum up, the power density, fuel utilization factor and fuel efficiency increase when anode pore size decreases.

As shown in Fig. 15, the temperature distribution of PEN structure is more uniform in the width direction of the cell stack with the decrease of anode porosity due to the better uniform of air flows. The temperature difference of PEN structure decreases in the width direction of the cell stack when anode porosity decreases, but increases with the increase of anode thickness. However, the temperature difference of PEN structure is almost constant with the decrease of anode pore size.

Fig. 16 shows the average temperature difference of PEN structure in the air flow direction for cases 4, 7–9. The temperature gradient of PEN structure falls down when anode porosity and anode thickness increase because of the increase of air ratio, whereas it is almost unchanged with the variation of anode pore size, as mentioned in Ref. [36]. This is because the heat transfer in the porous anode is dominated by the streamwise heat conduction, which is approximately proportional to the effective thermal conductivity defined in Eq. (18) when the cross-sectional area is constant. Therefore, the temperature distribution is independent of anode pore size. Moreover, the PEN structure temperature continuously rises along the air flow directions in the thicker anode

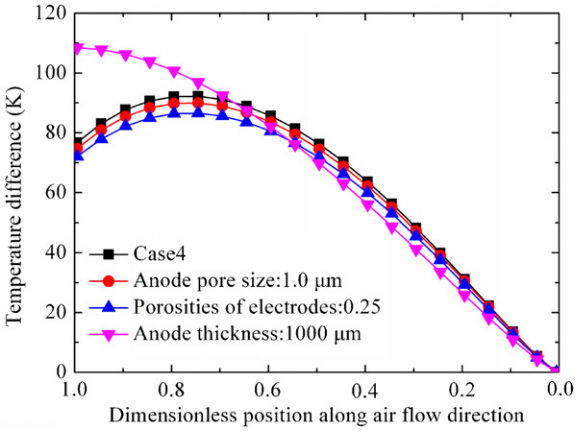

Fig. 16. Averaged temperature difference of PEN structure for counter flow in cases 4, 7–9 listed in Table 7.

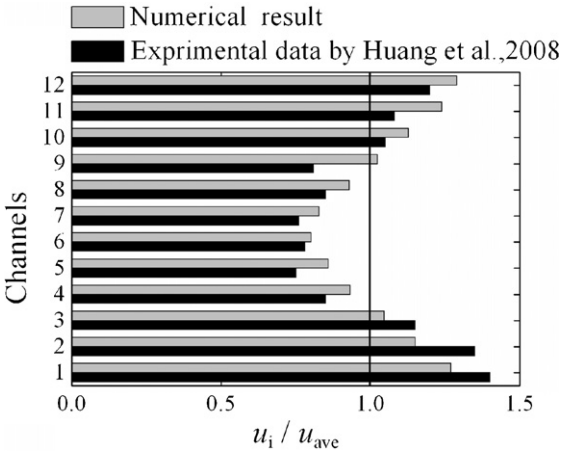

Fig. 17. Comparisons between the calculated flow velocity distributions and the experimental (u_{ave} is the averaged velocity of 12 channels).

case (case 9) because the lower heat transfer in thicker anode will weaken the cooling effect of fuel flows.

3.5. Validation

An important parameter used to control flow rates for the fluid flow channel, the hydraulic Reynolds number, $Re = u_{ave}D_h/\nu$, is defined, where u_{ave} is the averaged velocity from 12 rib-channels, ν is the kinematical viscosity of the fluid, and $D_h = 2Wd/(W + d)$ is the hydraulic diameter. Note that W and d are the width and height of the rib-channels.

In order to validate the numerical model developed in this paper, the numerical flow velocity data are compared with the experimental reported by Huang et al. [6]. The comparison between the calculated flow velocity distributions and the experimental is indicated in Fig. 17 by using water as the working fluid, where the value of flow Reynolds number is 170. As can be seen from Fig. 17, the present simulation results agree very well with the experimental and thus validate the present model. Their permissible difference may be caused by the different position and size of the gas inlets at the gas feed headers in the present model and the experimental by Huang et al. As mentioned in Ref. [6], the validated flow models can be established to simulate gaseous transport phenomena and electrochemical reactions in the one-cell stack.

4. Conclusions

Numerical simulation and modelling the heat and mass transfer and electrochemical reaction in the one-cell stack of planar SOFCs are carried out by using the temperature-dependent physical parameters of multi-components mixture gas and cell stack components. This study investigates the degree of flow uniformity in different cases with the variation of operating conditions and structural parameters and their influence to the cell stack performance. The major conclusions are listed as follows.

(1) Compared with the co-flow case, the counter flow case, offers the thermodynamic and electrochemical advantages in better uniform current density and temperature distributions of PEN structure in the width direction of the cell stack due to the relatively uniform air and fuel flows, as well as higher power output, fuel utilization factor and fuel efficiency.
(2) For counter flow case, it is effective to decrease the thermal gradient of PEN structure by increasing the air inlet delivery rate and decreasing the fuel inlet delivery rate. Moreover, better

performance (higher power output, fuel utilization factor and fuel efficiency) is achieved with lower fuel inlet delivery rate.

(3) For counter flow case, it is beneficial to obtain the better thermodynamic and electrochemical performance by increasing the air inlet temperature, when the cell stack operates on the condition that the ascending of the average temperature gradient of PEN structure is less than its descending. The temperature gradient of PEN structure drops with the decrease of fuel inlet temperature.

(4) For counter flow case, it is effective to improve the thermal gradient of PEN structure by decreasing the anode porosity due to the better uniform air flows. The power output, fuel utilization factor and fuel efficiency increase when anode pore size and thickness decrease. But the temperature distribution of PEN structure is almost constant when anode pore size decreases.

Acknowledgements

Authors gratefully acknowledge the contribution of the National Natural Science Foundation of China (Grant No. 50675081) and China Postdoctoral Science Foundation (Grant No. 20080440940).

References

[1] S.C. Singhal, Solid State Ion. 135 (2000) 305–313.
[2] S.C. Singhal, Solid State Ion. 152–153 (2002) 405–410.
[3] H. Yakabe, Y. Baba, T. Sakurai, M. Satoh, I. Hirosawa, Y. Yoda, J. Power Sources 131 (2004) 278–284.
[4] K.S. Weil, B.J. Koeppel, J. Power Sources 180 (2008) 343–353.
[5] L.K. Chiang, H.C. Liu, Y.H. Shiu, C.H. Lee, R.Y. Lee, Renew. Energy 12 (2008) 2580–2588.
[6] C.M. Huang, S.S. Shy, C.H. Lee, J. Power Sources 183 (2008) 205–213.
[7] Z. Lin, J.W. Stevenson, M.A. Khaleel, J. Power Sources 117 (2003) 92–97.
[8] P.W. Li, S.P. Chen, M.K. Chyu, J. Power Sources 140 (2005) 311–318.
[9] A. Smirnov, A. Burt, I. Celik, J. Power Sources 158 (2006) 295–302.
[10] A.C. Burt, I.B. Celik, R.S. Gemmen, A.V. Smirnov, J. Power Sources 126 (2004) 76–87.
[11] K.P. Recknagle, R.E. Williford, L.A. Chick, D.R. Rector, M.A. Khaleel, J. Power Sources 113 (2003) 109–114.
[12] S. Maharudrayya, S. Jayanti, A.P. Deshpande, J. Power Sources 144 (2005) 94–106.
[13] W.L. Huang, Q. Zhu, J. Power Sources 178 (2008) 353–362.
[14] P. Yuan, J. Power Sources 185 (2008) 381–391.
[15] J. Huang, C.K. Chen, D.Y. Ai, J. Power Sources 140 (2005) 235–242.
[16] M. Vinod, V. Janardhanan, O. Heuveline, Deutschmann, J. Power Sources 172 (2007) 296–307.
[17] T. Araki, T. Ohba, S. Takezawa, K. Onda, Y. Sakaki, J. Power Sources 158 (2006) 52–59.
[18] S. Bedogni, S. Campanari, P. Iora, L. Montelatici, P. Silva, J. Power Sources 171 (2007) 617–625.
[19] E. Achenbach, J. Power Sources 49 (1994) 333–348.
[20] S.B. Beale, Y. Lin, S.V. Zhubrin, W. Dong, J. Power Sources 118 (2003) 79–85.
[21] Y. Wang, F. Yoshiba, T. Watanabe, S. Weng, J. Power Sources 170 (2007) 101–110.
[22] J. Yuan, M. Rokni, B. Sunden, Numer. Heat Transf. A: Appl. 43 (2003) 341–366.
[23] Vinod M. Janardhanan, O. Deutschmann, J. Power Sources 162 (2006) 1192–1202.
[24] N. Autissier, D. Larrain, J. Van herle, D. Favrat, J. Power Sources 131 (2004) 313–319.
[25] R. Bove, S. Ubertini, J. Power Sources 159 (2006) 543–559.
[26] P.A. Ramakrishna, S. Yang, C.H. Sohn, J. Power Sources 158 (2006) 378–384.
[27] Q. Wang, C. Wang, B. Ren, L. Li, Energy Eng. 126 (2007) 16–21 (in Chinese).
[28] Q. Wang, B. Ren, L. Li, B. Gao, J. Therm. Sci. Technol. 5 (2006) 339–345 (in Chinese).
[29] Q. Wang, L. Li, C. Wang, J. Power Sources 186 (2009) 399–407.
[30] G. Wang, Y. Yang, H. Zhang, W. Xia, J. Power Sources 167 (2007) 398–405.
[31] Y. Yang, G. Wang, H. Zhang, W. Xia, J. Power Sources 177 (2008) 426–433.
[32] Y. Yang, G. Wang, H. Zhang, W. Xia, J. Power Sources 173 (2007) 233–239.
[33] G. Wang, Y. Yang, H. Zhang, Proc. CSEE 27 (2007) 99–103 (in Chinese).
[34] H. Yakabe, T. Ogiwara, M. Hishinuma, I. Yasuda, J. Power Sources 102 (2001) 144–154.
[35] Fluent 6. 3 User's Guide, Fluent Inc., 2006.
[36] J. Yuan, M. Rokni, B. Sundén, J. Heat Transf. 127 (2005) 1380–1390.
[37] H. Yakabe, M. Hishinuma, M. Uratani, Y. Matsuzaki, I. Yasuda, J. Power Sources 86 (2000) 423–431.
[38] M. Suzuki, N. Shikazono, K. Fukagata, N. Kasagi, J. Power Sources 180 (2008) 29–40.
[39] S.H. Chan, K.A. Khor, Z.T. Xia, J. Power Sources (93) (2001) 130–140.